Available online at www.sciencedirect.com
ScienceDirect
Earth and Planetary Science Letters 259 (2007) 384–399
EPSL
www.elsevier.com/locate/epsl

Inclusions of nanocrystalline hydrous aluminium silicate "Phase Egg" in superdeep diamonds from Juina (Mato Grosso State, Brazil)

Richard Wirth [a,*], Christian Vollmer [b], Frank Brenker [c], Stanislav Matsyuk [d], Felix Kaminsky [e]

[a] *GeoForschungsZentrum Potsdam, Department "Chemistry of the Earth", Telegrafenberg, D 14473 Potsdam, Germany*
[b] *Max Planck Institute for Chemistry, Joh.-J.-Becher Weg 27, D 55020 Mainz, Germany*
[c] *JWG University, Institute for Mineralogy, Senckenberganlage 28, D 60054 Frankfurt am Main, Germany*
[d] *Institute of Geochemistry, Mineralogy and Ore Formation, National Academy of Sciences of Ukraine, Palladin Av., 03680 Kyiv-142, Ukraine*
[e] *KM Diamond Exploration Ltd., 2446 Shadbolt Lane, West Vancouver V7S 3J1, B.C., Canada*

Received 4 January 2007; received in revised form 5 April 2007; accepted 29 April 2007
Available online 8 May 2007
Editor: C.P. Jaupart

Abstract

Inclusions in alluvial diamond from Juina (Mato Grosso, Brazil) have been investigated by TEM methods (electron diffraction, HRTEM, AEM, HAADF, EELS) and Raman spectroscopy. The inclusion paragenesis of Juina diamonds is dominated by ultrahigh-pressure ("superdeep") phases. One of these diamonds, sample #1.1/4, contains several micrometer-sized (approximately 200 μm by 50–70 μm) inclusions, which have been studied. TEM foils prepared applying Focused Ion Beam (FIB) technique revealed that these inclusions consist of a porous, nanocrystalline groundmass, which is composed of nanometre-sized crystals of a hydrous aluminium silicate phase with Al:Si approximately 1:1 and chemical composition of phase "Egg" ($AlSiO_3(OH)$), a minor volume fraction of nanocrystalline stishovite and pore space, which was originally filled with a fluid or gas. The nanocrystalline hydrous aluminium silicate phase is idiomorphic, randomly oriented (approximately 20–30 nm in size) predominantly with tetragonal crystal structure (a_0=0.743 nm, c_0=0.706 nm). The monoclinic structure of synthetic phase "Egg" determined at ambient conditions [M.W. Schmidt, L.W. Finger, R.J. Ross, R.E. Dinnebier, Synthesis, crystal structure, and phase relations of $AlSiO_3OH$, a high-pressure hydrous phase, American Mineralogist 83 (1998) 881 – 888] is only occasionally observed. The fluid filling in the porosity has been released into the vacuum of the FIB during TEM specimen preparation. Quench products of the fluid containing minor concentrations of F- P- S- Cl- K- Ca and Ba were detected at the walls of the pores. In addition phase "Egg" is identified by μ-Raman spectroscopy within a second sample (RS 43a) from the same location. The presence of Phase "Egg" in the inclusions in diamond may suggest that crustal material has been subducted to a depth of the lower Transition Zone. Although, metastable growth of nanocrystalline high-pressure phases or extension of their respective stability fields to lower pressure can not ruled out completely.

Keywords: diamond; inclusion; TEM; mantle; subduction; crustal material

* Corresponding author. Tel.: +49 331 2881319; fax: +49 331 288 1402.
E-mail address: wirth@gfz-potsdam.de (R. Wirth).

0012-821X/$ - see front matter © 2007 Elsevier B.V. All rights reserved.
doi:10.1016/j.epsl.2007.04.041

1. Introduction

Slab subduction transports crustal components such as sediments and basalts into the Earth's interior. A still debated question is how deep crustal material can be subducted. Subduction depths of more than 130 km are documented in ultrahigh-pressure rocks from Dabie Shan (Okay, 1993). Various hydrous minerals in the descending slabs can transport water into the Earth's mantle. Phase "Egg", $AlSiO_3OH$ is a potential candidate for a water-bearing mineral in Al-rich sediments or hydrous basalts, which is stable even at the depth of the Transition Zone. Experiments in the system Al_2O_3–SiO_2–H_2O have shown that hydrous aluminium silicates are stable at very high-pressures and temperatures. Depending on the P–T conditions, different hydrous aluminium silicates exist. In the pressure range from 2 GPa to 6 GPa, phase Pi $Al_3Si_2O_7(OH_3)$ is stable (Wunder et al., 1993a). Above 5 GPa, topaz-OH $Al_2SiO_4(OH)_2$ was reported (Wunder et al., 1993b). Phase "Egg" $AlSiO_3(OH)$ with an Al:Si ratio 1:1 was observed at pressures exceeding 10 GPa and at about 1000 °C (Eggleton et al., 1978). The crystal structure of phase "Egg", including the position of the hydrogen, has been solved from high-resolution X-ray powder diffraction at ambient conditions. The resulting monoclinic cell is based on lattice parameters: a_0=0.7144 nm, b_0=0.4335 nm, c_0=0.6952 nm and the monoclinic angle β=98.396°; space group is $P2_1/n$ (Schmidt et al., 1998). The high temperature stability limit of phase "Egg" $AlSiO_3OH$ was determined in a pressure range from 7 to 20 GPa and at a temperature range from 900 to 1700 °C (Ono, 1999). A more recent investigation of the stability conditions of Phase "Egg" and aluminium oxide hydroxide δ-AlOOH finally clarified that Phase "Egg" is stable at least up to 1625 °C at 17 GPa (Sano et al., 2004). The upper temperature limit of phase "Egg" is controlled by the reaction: Phase "Egg"=stishovite+corundum+fluid. Decomposition of Phase "Egg" into δ-AlOOH and stishovite occurs at pressures greater than 23 GPa below the Transition Zone without any water release. At temperatures above 1200 °C at 23 GPa phase "Egg" decomposed into corundum+stishovite+fluid (Sano et al., 2004). The compressibility of phase "Egg", its equation of state up to 40 GPa, and the role of water at high pressure were reported in a recent paper (Vanpeteghem et al., 2003). NMR measurements of Phase "Egg" revealed that the Si–Al distribution in phase "Egg" is partially disordered. The observed structural disorder and hydrogen bonding is suggested to be responsible for the high upper temperature limits (1500–1700 °C) of phase "Egg" (Xue et al., 2006).

In recent decades, superdeep diamonds originating within the lower mantle and Transition Zone have been reported from South Africa, Australia, USA, Canada, Guinea, Venezuela and Brazil (Scott-Smith et al., 1984; Otter and Gurney, 1989; Davies et al., 1999; Stachel et al., 2000; Kaminsky et al., 2000; Brenker et al., 2002; Brenker et al., 2005; Kaminsky et al., 2006). Of particular interest are superdeep diamonds from the Juina area in Mato Grosso State, Brazil, which mostly comprise alluvial diamond crystals. These diamond crystals contain a large number of syngenetic, superdeep mineral inclusions that include some new mineral phases not previously observed in crustal and upper mantle associations (Wilding et al., 1991; Harte and Harris, 1994; Harris et al., 1997; Harte et al., 1999; Hutchison et al., 2001; Kaminsky et al., 2001; Hayman et al., 2005). Among those mineral inclusions are: Fe-periclase, CaSi-walstromite (former CaSi-perovskite), low Ni enstatite (former MgSi-perovskite), majoritic garnet, TAPP (tetragonal almandine pyrope phase), and a SiO_2 phase with unknown structure.

The objective of this study was to investigate a new collection of diamond crystals from the Juina area, in order to find new superdeep mineral inclusions and to determine their crystal structure.

As a result of this work, we herein document the first natural occurrence of phase "Egg"+stishovite as nanometre-sized, porous inclusions in diamond. The presence of OH-groups in the $AlSiO_3OH$ was also established.

2. Sample description and analytical techniques

The inclusion paragenesis of Juina diamonds is dominated by ultrahigh-pressure ('superdeep') phases (Kaminsky et al., 2001; Hayman et al., 2005). Ten new diamond crystals from alluvial sediments in the Juina area were selected for analysis; one of these contained a visible ilmenite inclusion (sample #1.1). The investigated diamond sample labelled sample #1.1/4 is part of a crushed diamond containing an ilmenite inclusion that has already been described (Kaminsky et al., 2001).

All inclusions in diamond reported in the present study have been investigated by transmission electron microscopy (TEM) techniques such as electron diffraction, analytical electron microscopy (AEM), electron energy-loss spectroscopy (EELS) and high-resolution electron microscopy (HREM). In addition, several diamonds were studied by confocal μ-Raman spectroscopy before the release of the inclusion.

In order to compare crystallographic and chemical parameters of the newly discovered natural Phase "Egg" with synthetic Phase "Egg" $AlSiO_3(OH)$ we used powder material that was synthesized using high-pressure techniques. Bernd Wunder performed the synthesis in a split-sphere multi-anvil press at the Bayerisches Geoinstitut,

Bayreuth. Experimental conditions were identical to those previously described in the literature (16 GPa/1000 °C/15 h) (Eggleton et al., 1978). X-ray powder diffraction of the same synthesis products confirmed the presence of phase 'Egg', stishovite, and traces of an unknown phase.

2.1. TEM sample preparation

Electron-transparent foils were prepared by focused ion beam (FIB) techniques. FIB allows preparation of site-specific TEM foils with typical dimensions of 15–20 μm in width, approximately 10 μm in height and approximately 0.150 μm in thickness. In the case of diamond, the sample thickness can be greater, up to 0.300 μm, because of the low electron absorption of diamond. Thicker foils have the advantage that some of the nanometre-sized inclusions might remain closed and their content will then be accessible to X-ray analysis. A focused Ga-ion beam is used to sputter material from the sample, resulting in a thin, electron-transparent foil. A special device called a selected carbon mill (SCM)™ significantly enhances the sputtering process of diamond, which is slow compared to silicates. SCM uses OH-containing $MgSO_4$, which is heated inside the SCM device. The released water vapour is brought close to the ion beam by inserting a needle near to the location where the foil will be cut. H_2O decomposes by the ion beam and oxygen oxidises the diamond. Details of the FIB technique and the use of SCM are described elsewhere (Wirth, 2004).

TEM investigations were performed with a TECNAI F20 XTWIN transmission electron microscope operating at 200 kV with a field emission gun electron source. The TEM is equipped with a Gatan Tridiem™ filter, an EDAX Genesis™ X-ray analyzer with ultrathin window and a Fishione high angle annular dark field detector (HAADF). The Tridiem filter was used for the acquisition of energy-filtered images applying a 20 eV window to the zero loss peak. EEL spectra were acquired with a dispersion of 0.1 eV/channel. The resolution of the filter was 0.9 eV at half width, at full maximum of the zero loss peak. Acquisition time was 1 s with a 2 mm entrance aperture of the filter. Spectra of the oxygen K-edge were acquired in diffraction mode.

EDX spectra were usually acquired in the scanning transmission mode (STEM) using the TIA™ software package of the TEM. Significant mass loss during analysis was avoided by scanning the beam in a pre-selected window (20×20 nm or larger). Spot size was approximately 0.1 nm, and acquisition time 60 s at an average count rate of 60–80 counts/s. This resulted in a counting error of about 4–5% at a 3σ level. Several analyses were performed in TEM mode on the same inclusion that was imaged at high-resolution. For these measurements spot size 8 (spot diameter focused is approximately 0.1 nm) was used at slightly defocused conditions in a way that the beam just circumscribes the nanoinclusions. Some of the nanoinclusions have been imaged at high resolution, and EDX and EEL spectra were acquired from these nanocrystals after the high-resolution imaging.

2.2. Raman spectroscopy

Raman analyses were carried out by means of a Jobin Yvon LabRam HR system (focal length 800 mm) equipped with Olympus BX41 optical microscope and a Renishaw RM-1000 μ-Raman spectrometer. Both instruments operate with a grating of 1800 grooves/mm in the optical path, and Si-based charge-coupled device detectors. Spectra were excited with a red He–Ne (633 nm) and a green YAG (532 nm) Laser. The wavenumber accuracy was about 0.5 cm^{-1} and the spectral resolution 0.8 cm^{-1}. The lateral and depth resolution was on the order of several to a few tens of μm depending on the actual sampling depth.

3. Results

3.1. TEM studies

Fragments of a crushed diamond (sample #1.1/4) contain several lath-shaped inclusions that are approximately

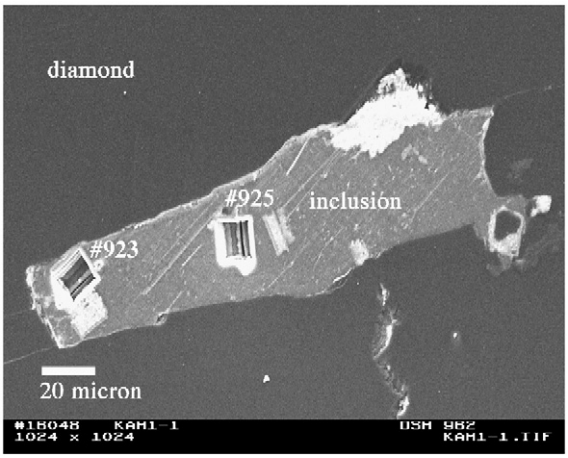

Fig. 1. Back-scatter electron (BSE) image of one of the inclusions in diamond. Two locations of TEM foil preparation (#923, #925) applying focused ion beam (FIB) technique are visible. The inclusion consists of nanocrystalline $AlSiO_3OH$ phase "Egg" and a small volume fraction of SiO_2 stishovite+porosity (filled with a fluid). The fluid was released to the vacuum during foil preparation. The surface feature below the inclusion represents the end of another inclusion with the material removed during the polishing.

200 μm by 50–70 μm. One of the inclusions is illustrated in Fig. 1. Two FIB cutting sites of TEM foils (#923, #925) are displayed. The surface roughness exposed below the inclusion is not a crack but the end of another inclusion from which material has been removed during the polishing process. Ten individual TEM foils have been prepared by FIB from different locations in different inclusions of the same sample (#887, #888, #903, #913, #923, #925, #926, #975, #976, #1040). The foils are approximately 15 μm wide, 10 μm high and 0.200–0.100 μm thick. TEM investigation of all of theses foils shows that the inclusion consists of a porous crystalline

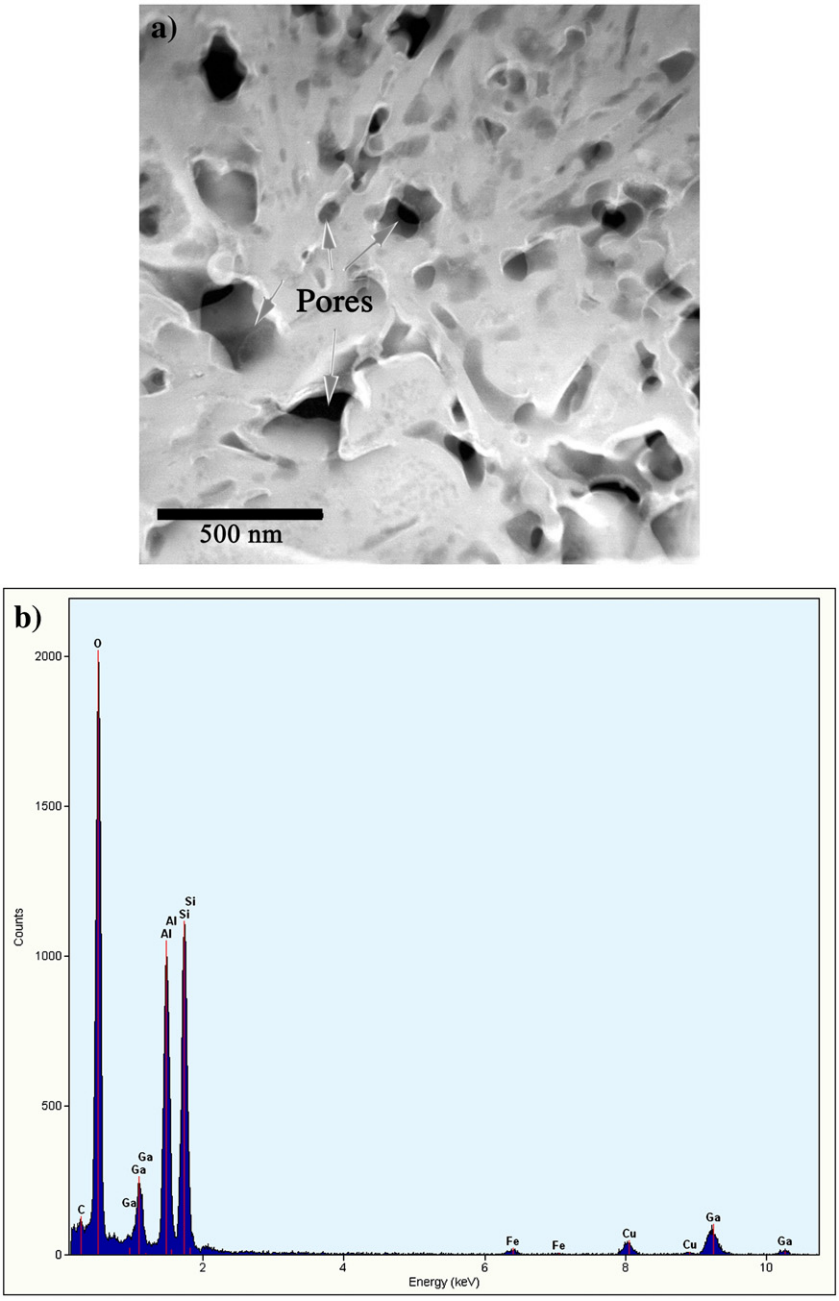

Fig. 2. a) STEM image (high angle annular dark filed detector (HAADF)) of the inclusion in diamond showing a porous structure (dark rounded areas) in a fully crystalline matrix (bright contrast), which consists of nanocrystalline $AlSiO_3OH$ phase "Egg" and stishovite. b) Corresponding energy dispersive X-ray intensity spectrum from the whole image. Gallium intensity in the spectrum is due to FIB preparation and Cu intensity is due to X-ray intensity from the copper grid.

matrix material (Fig. 2a), which is sensitive to electron irradiation damage, indicated by decreasing diffraction contrast with increasing exposure time. The nanoinclusions that form the matrix are mainly composed of aluminium, Si, oxygen, and minor iron (Al(K)=48.6 at.%, Si (K)=50.8 at.% and Fe(K)=0.6 at.%). The Al:Si intensity ratio equals approximately 1:1 (Fig. 2b). The weak X-ray intensities of Cu–K_α and Ga–K_α as well as Ga–L in the spectrum are due to the copper grid and some Ga implanted during foil preparation. TEM bright field as well as dark field images show that the matrix consists of nanometre-sized crystalline inclusions (Fig. 3a,b), which are randomly distributed and oriented in the matrix. The random orientation of the individual nanocrystals is documented in the Debye–Scherrer ring electron diffraction pattern inserted in Fig. 3a. The random crystallographic orientation of the individual crystals is the reason why only a few of them are visible in dark field imaging. However, high-resolution imaging documents that the matrix is fully crystalline. The matrix of the inclusion is basically composed of these nanocrystals. High-resolution images of these crystals exhibit their idiomorphic shape with approximately square cross section and an average diagonal length of 20–30 nm (Fig. 4). The grain size of individual nanocrystals in one and the same inclusion varies within a given inclusion. Foil #926 from the same inclusion but from a different location exhibits nanoinclusions with the same chemical composition (Al(K) =49.1 at.%, Si(K)=50.3 at.%, Fe(K)=0.6 at.%) as the nanocrystalline crystals but with significantly larger grain size. The grains are lath-shaped, up to 500 nm long and 200–300 nm wide (Fig. 5a). The Al:Si intensity ratio again is approximately 1:1 (Fig. 5b). The large grains exceed the thickness of the foil (about 200 nm) thus providing X-ray intensities which are probably not influenced by any matrix effects.

In addition to the large, lath-shaped crystals, about 18 individual nanocrystals were analysed after HREM imaging using a defocused beam. It proved crucial to defocus the beam (spot size focused about 0.1 nm) to avoid mass loss during the measurement. This was achieved by widening the beam to the diameter of the nanocrystals (about 20–30 nm). All of the grains were of the same composition with identical Al:Si intensity ratios of approximately 1:1 (Fig. 6a). The results of analytical electron microscopy (AEM) are given in Table 1.

In several cases, it was possible to acquire, additionally to the EDX spectrum, an EEL spectrum from the same nanocrystal. The oxygen K-edge at 532 eV of the nanocrystal always shows a small pre-peak at approximately 528 eV (Figs. 5c and 6c), which is indicative of the presence of OH-groups (Wirth, 1997). The chemical composition of the nanocrystals suggests them to be water-containing aluminium silicates with an Al: Si ratio of approximately 1:1. The only known high-pressure phase with such a chemical composition is synthetic phase “Egg” (Eggleton et al., 1978; Schmidt et al., 1998; Ono, 1999; Sano et al., 2004). A comparison of the chemical composition with AEM of the observed nanocrystals with synthetic phase “Egg” (synthesized by B. Wunder) shows that both phases display the same

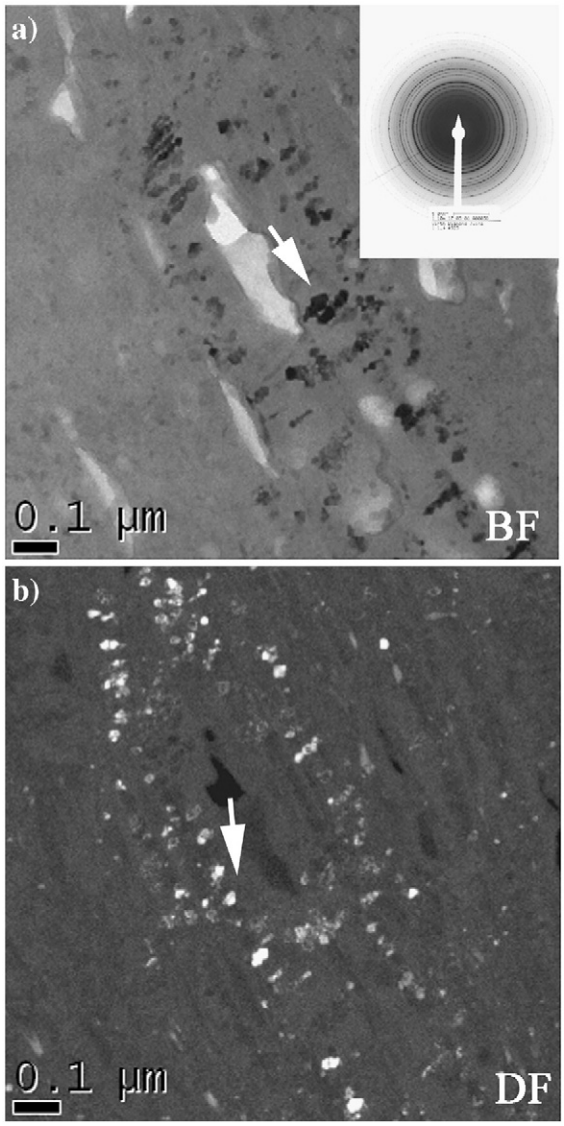

Fig. 3. Energy-filtered TEM bright field (BF) and dark filed images (DF) demonstrating that the inclusions are composed of randomly oriented nanocrystals. a) BF image displaying the nanocrystals of $AlSiO_3OH$ phase “Egg” in dark contrast (arrow). White elongated contrast characterizes porosity. b) DF image showing the nanocrystals of phase “Egg” in bright contrast (arrow).

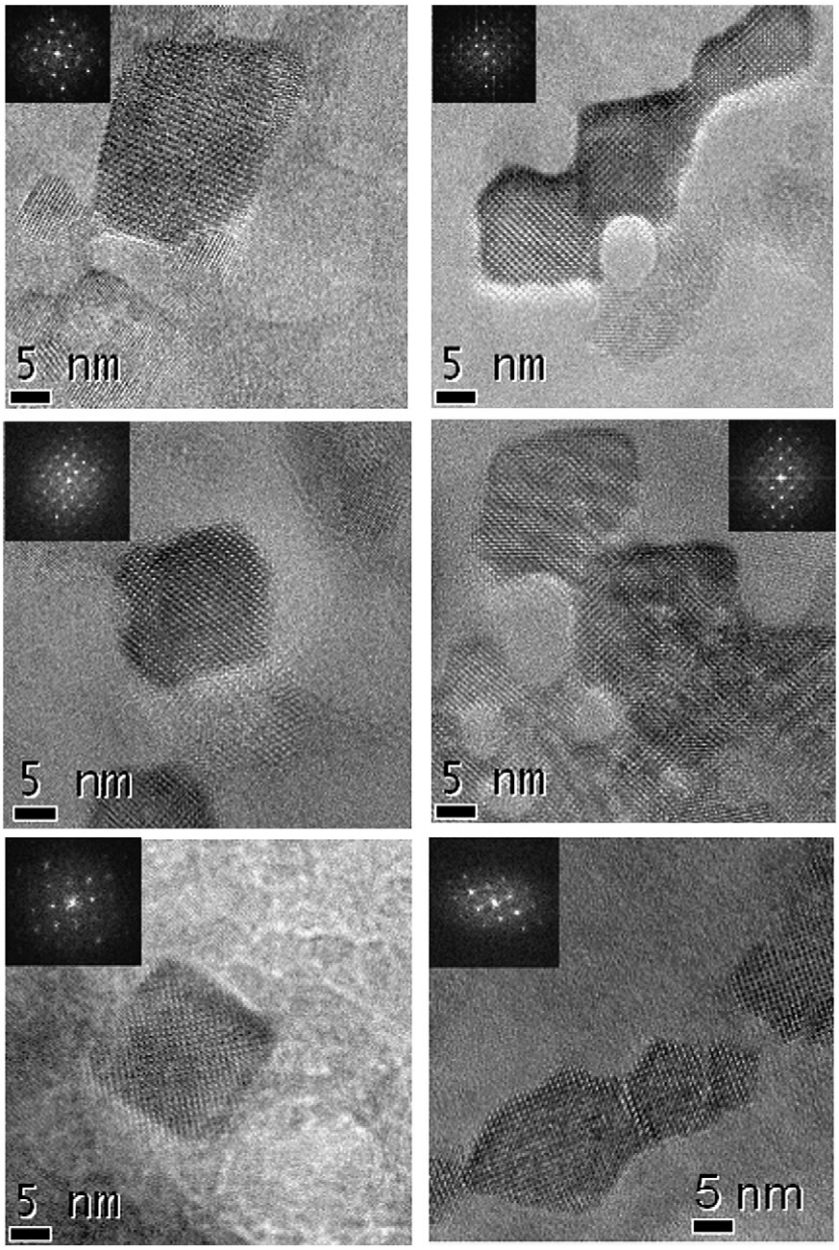

Fig. 4. Energy-filtered high-resolution images of different nanoinclusions of $AlSiO_3OH$ phase "Egg" with the corresponding calculated diffraction patterns (fast Fourier Transforms FFT) inserted.

pre-peak in the EEL spectrum at the same position and with similar intensity, and that they have the same Si:Al ratio of approximately 1:1 (Fig. 6a,b).

Elemental maps of the inclusions, which record a full spectrum pixel by pixel, allow subsequent evaluating the maps pixel by pixel. Such a procedure reveals that there are regions that show high Si concentrations combined with low Al concentration. EDX window analyses of those indicated locations suggest that at least one additional phase, primarily composed of silicon and oxygen with minor Al, is present in the matrix (Fig. 7a,b,c). It cannot be excluded that the Al concentration is a matrix effect due to the presence of phase "Egg" in the vicinity. However, stishovite might contain Al_2O_3, and the Al_2O_3 content increases with temperature (Ono, 1999; Sano et al., 2004). The silica inclusions are of similar size (about 20 nm) to the nanoinclusions described above and often display a sphere-like shape. The composition of this SiO_2-rich

phase suggests that this phase might be stishovite or coesite. The stishovite crystal structure is proved by the electron diffraction pattern containing stishovite d_{hkl} spacing such as 0.295 nm $(110)_{stish}$, 0.224 nm $(101)_{stish}$, 0.209 nm $(200)_{stish}$. They are observed in the selected area electron diffraction patterns only but never in the calculated diffraction pattern (Fast Fourier Transform FFT) from individual nanocrystals of Phase "Egg" (cf. Table 2). Selected area electron diffraction patterns sample a much larger volume than the HREM images, and thus

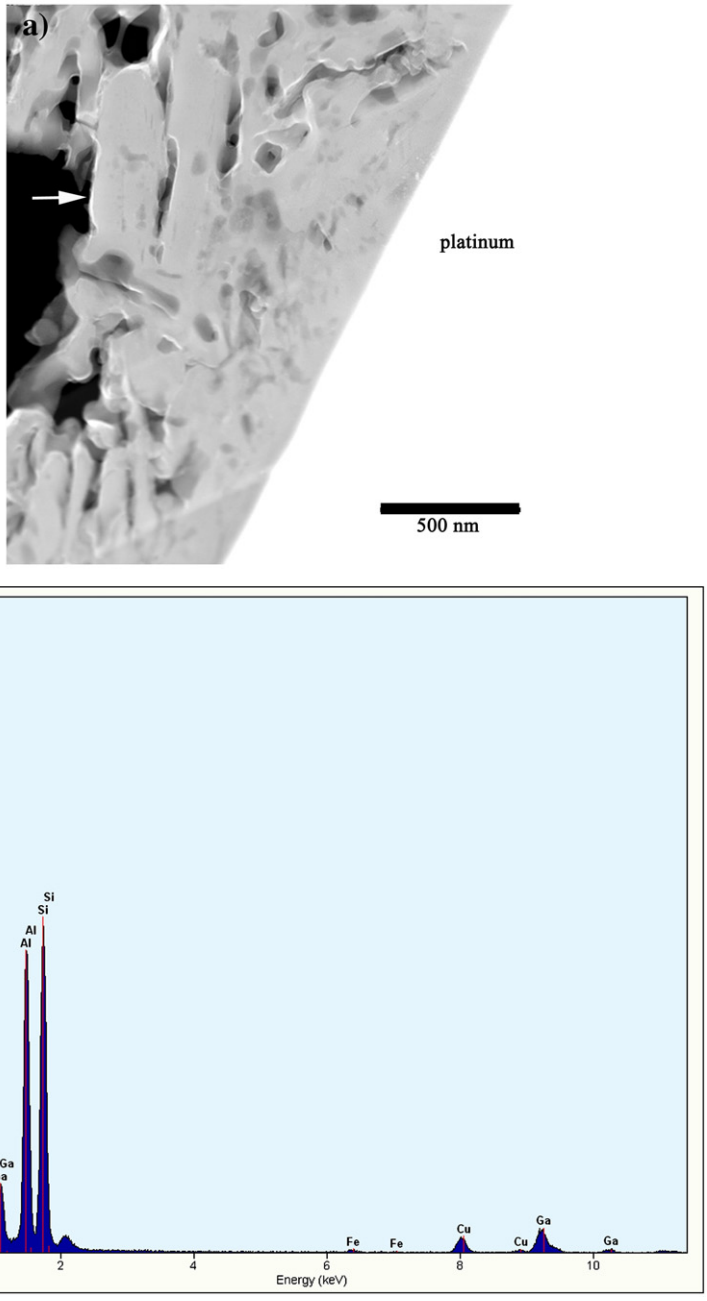

Fig. 5. a) STEM (HAADF) image of a coarse grained inclusion with lath-shaped crystals. Dark contrast represents porosity b) X-ray intensity spectrum of the lath-shaped crystal indicated by an arrow in a). c) Electron energy-loss spectrum (EELS) showing the oxygen K-edge of the lath-shaped crystal with a pre-peak at about 528 eV indicating the presence of OH in the crystal. The upper curve shows the original spectrum and the lower curve the background subtracted spectrum with the background fit region indicated.

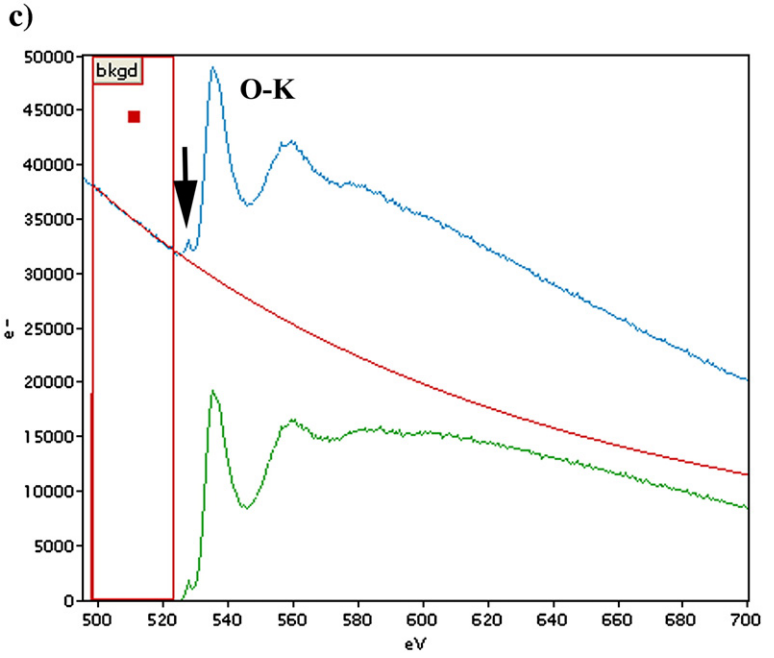

Fig. 5 (*continued*).

make it more likely to identify the presence of a minor phase such as stishovite.

Crystal structure data of the nanoinclusions were derived from selected area diffraction patterns (cf. insert Fig. 3) and from fast Fourier Transforms (FFT), which are calculated from energy-filtered high-resolution images using the Gatan Digital Micrograph software package. The sensitivity to electron irradiation damage prevented the application of convergent beam electron diffraction techniques. Cell parameters were deduced from 18 individual nanometre-sized single crystals oriented with a low index zone axis parallel to the electron beam and more than 53 randomly oriented crystals. From all these data, two major cell parameters with a_0=0.743 nm (100) and c_0=0.706 nm (001) with the resulting vector [101]= 0.511 nm were derived. The angle between these two major axes is 90° within the accuracy of the measurement of angles at the monitor. In Fig. 8, another nanocrystal is shown with the two major axes a_0 and b_0 of the same length (approximately 0.733 nm) and the resulting vector [110]=0.518 nm. All measured d_{hkl} spacings derived from HREM images and from selected area electron diffraction patterns are presented in Table 2.

According to (Schmidt et al., 1998), the crystal structure of synthetic phase "Egg" is monoclinic with lattice parameters a_0=0.714 nm; b_0=0.433 nm; c_0=0.695; β=98.4°. We observed only one individual nanocrystal that displayed an angle of 98° between principal axes a_0 and c_0. In Table 2 the first column displays the d_{hkl} values calculated from the observed cell parameters assuming a tetragonal structure. A comparison of the observed d_{hkl} spacing deduced from HREM images and those from electron diffraction pattern with the d_{hkl} data from literature (monoclinic cell) shows that the tetragonal structure matches the experimental data much better. The d_{hkl} spacing 0.446 nm was observed in the calculated diffraction patterns as well as in the selected area diffraction patterns. However, this d-value is a forbidden reflection in monoclinic space group $P2_1/n$ (c.f. Table 2). The measured angles between the observed principal axes in a tetragonal lattice (0.7435 nm, 0.706 nm) and the resulting vector [101] are 45.1° and 44.2° respectively (mean values from 18 measurements). However, the angle between a_0 and c_0 in case of monoclinic phase "Egg" is 98.4° and the angles between the resulting vector [101] and the principle axes are 50.1° and 48.3° respectively. The generally absent d spacing of 0.446 nm in FFT and electron diffraction pattern, and the different angles observed suggest a crystal structure other than the monoclinic.

In some cases nanocrystals with the major axes (a_0 and b_0) having the same length were observed [Fig. 8]. Therefore, we concluded a tetragonal structure based on a unit cell with a_0=0.7435 nm and c_0=0.706 nm, and calculated the resulting d_{hkl} lattice spacing using the Desktop Microscopy™ software package. The calculated

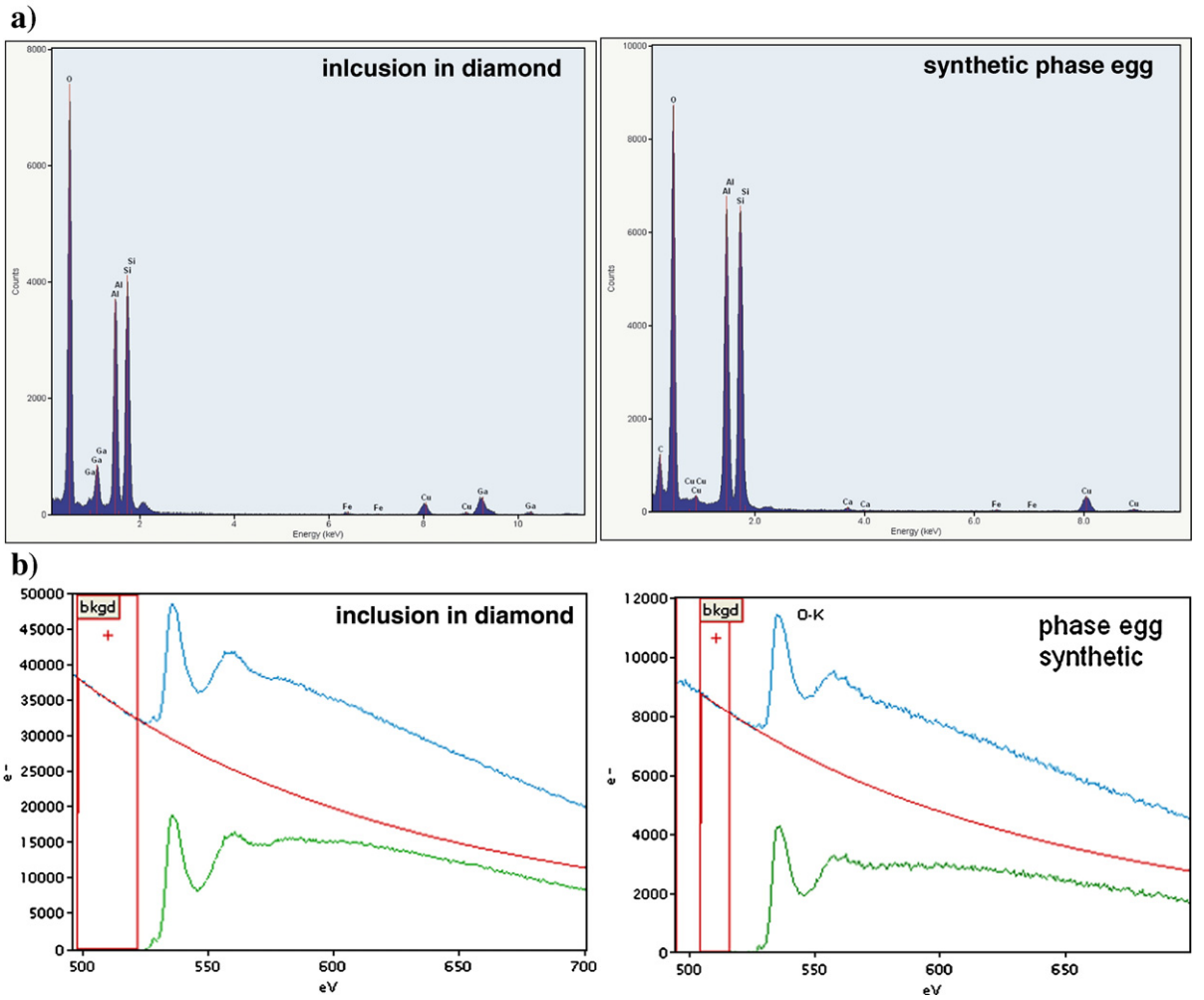

Fig. 6. a) X-ray intensity spectrum of an $AlSiO_3OH$ phase "Egg" nanocrystal compared with the spectrum of synthetic phase "Egg". b) Comparison of the EEL spectra in the region of the oxygen K-edge of the inclusion in diamond with synthetic phase "Egg".

d_{hkl} data fit the observed d_{hkl} values much better than those based on a monoclinic structure (c.f. Table 2). The calculated angles between a_0, c_0 and the resulting vector [101], based on a tetragonal structure, is 43.6° and 46.4° respectively. These angles match the observed angles 45.1° and 44.2° more closely. They deviate significantly from those angles in a monoclinic cell (50.1° and 48.3°) At this point, it should be emphasized that the structure determination of phase 'Egg' was carried out at ambient conditions. Hence, the discrepancy between the observed

Table 1
Chemical composition of nanoinclusions from different TEM samples from different inclusions in diamond 1.1/4 measured with AEM

	#976 at.%	#976 at.%	#975 at.%	#975 at.%	#926 at.%	#926 at.%	#923 at.%	#923 at.%	#923 at.%	#923 at.%	#903 at.%	#888 at.%	#882 at.%	Synthetic Phase Egg	Synthetic Phase Egg
Al(K)	47.57	49.68	49.90	53.84	49.08	48.08	48.60	49.16	47.72	46.74	48.00	48.34	49.08	50.46	51.80
Si(K)	51.74	49.98	49.21	45.63	50.31	51.62	50.82	51.05	51.66	52.60	52.00	50.14	50.31	49.12	47.74
Fe(K)	0.68	0.33	0.88	0.53	0.61	0.29	0.58	0.52	0.62	0.66	0.00	1.52	0.61		
Ca(K)														0.42	0.45
(Al+Fe)/Si	0.932	1.000	1.032	1.113	0.988	0.937	0.968	0.973	0.936	0.901	0.923	0.994	0.988	–	–
(Al+Ca)/Si														1.036	1.094

(#xxx TEM sample number or FIB prepared foil number).

tetragonal structure and the monoclinic structure given in literature for phase "Egg" will be discussed further below.

The results of this study show that the investigated inclusion in diamond sample 1.1/4 is composed of a porous matrix consisting of tetragonal nanocrystalline hydrous aluminium silicate with an identical chemical composition identical to that of synthetic phase "Egg", and minor stishovite. The crystal structure of the observed hydrous aluminium silicate is predominantly tetragonal with only one observed nanocrystal exhibiting a monoclinic

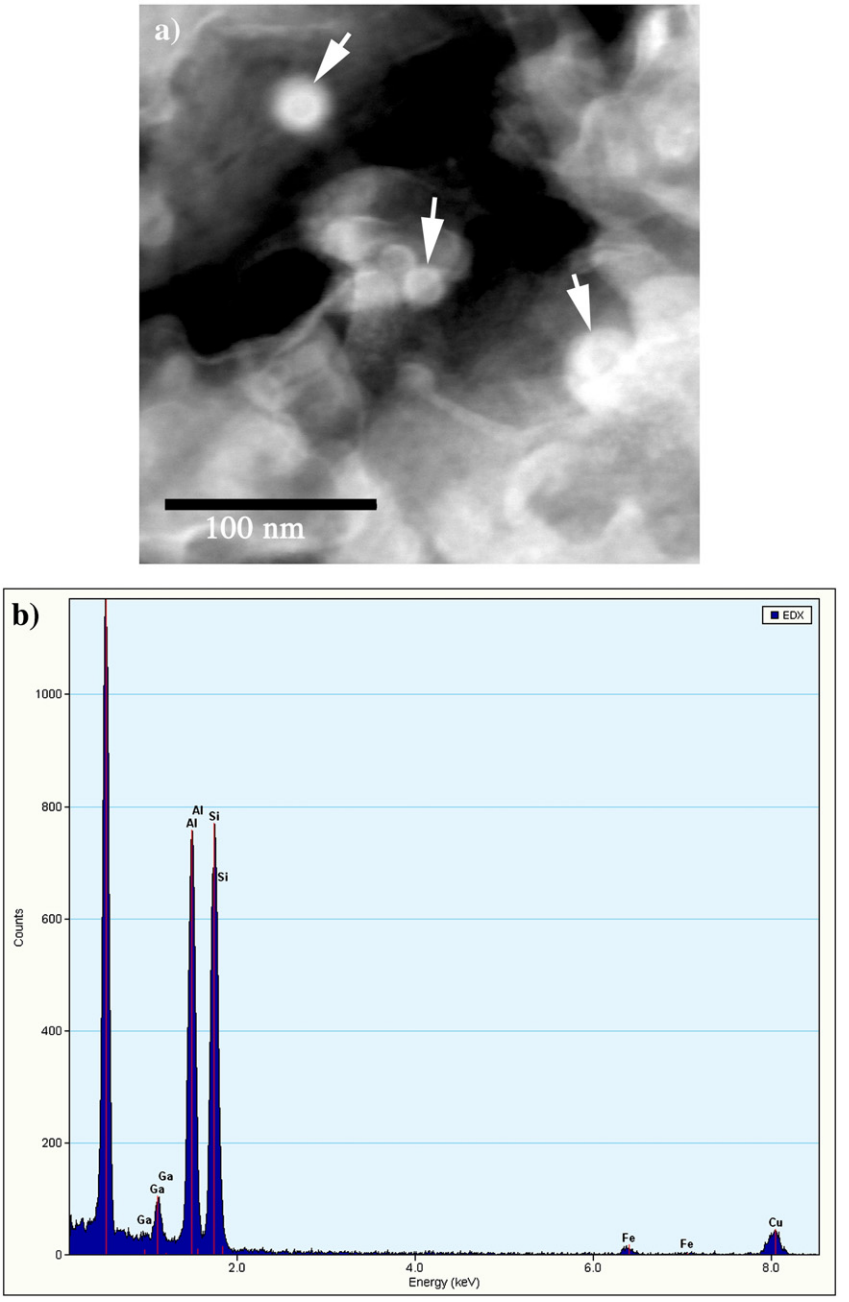

Fig. 7. a) STEM (HAADF) image of spherical nanoinclusions of stishovite in a matrix of phase egg. The extraordinary brightness of the spheres results from contamination due to a very small probe size (<1 nm) during the spectrum acquisition. The spectrum displays a high carbon peak due to contamination. The HAADF image was acquired after EDX spectrum acquisition. b) Chemical composition of the matrix corresponding to that of phase "Egg". c) Chemical composition of the nanospheres displaying mainly Si and oxygen with traces of Ca and some fluorine. The low Al intensity might be due to the Al-rich matrix; calcium and fluorine are supposed to be quench products along the pore walls or on the surface of the spheres.

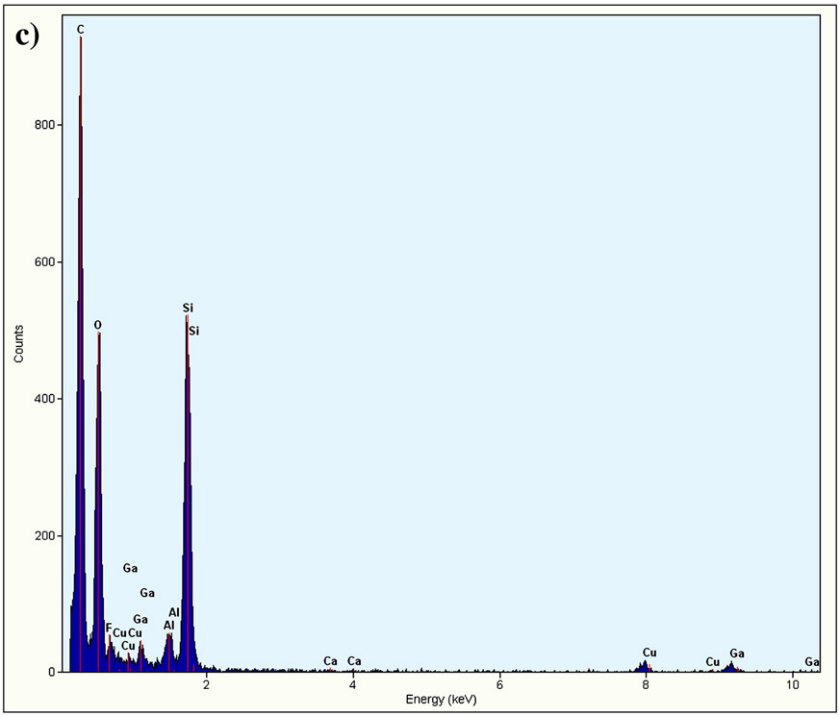

Fig. 7 (*continued*).

structure. The porous microstructure of the inclusions requires the presence of a fluid or gas phase during the formation of the inclusion, which has been released during FIB sample preparation. AEM analyses of larger volumes of an inclusion (window analysis covering an area of about 500 nm * 500 nm) including pores indicate the presence of minor concentrations of fluorine, phosphorous, sulphur, chlorine, potassium, calcium, barium and water, which are considered to be quench products of the fluid trapped in the pores.

3.2. Raman spectroscopy

A larger set of diamonds from the same area were screened for the presence of dense hydrous minerals. Beside the detection of several high-pressure phases, like CaSi-walstromite and coesite, the study yields around 30 new Raman spectra which did not match to any tabulated mineral phase of available Raman databases or the literature. In one case we found a complex spectrum with numerous Raman bands in the spectral range between 200 and 1200 cm^{-1} using the red 633 nm laser. The observed Raman bands show a good agreement with recently published spectra of phase "Egg" (Fig. 9, Table 3) (Xue et al., 2006). Most of the bands above a Raman shift of 360 cm^{-1} fit well with the peak position and relative intensity. Only in the low shift region Raman bands at 238, 291 and 313 cm^{-1} show no equivalent peak position of phase "Egg". The Raman band at 238 cm^{-1} is probably linked to the occurrence of stishovite which was identified together with phase "Egg" during our TEM studies. Small deviations between the synthetic phase "Egg" (Xue et al., 2006) and our measurements are most likely linked to the minor element chemistry, e.g. the Fe-content and the structural differences documented during our detailed TEM work. Any residual pressure on the inclusion will shift the respective peak position.

In order to further constrain the finding of phase "Egg" we examined the same inclusion in the OH-stretching region between 1800 and 3000 cm^{-1} with a 532 nm Laserbeam. Again a good correlation between inclusion No RS-43a and synthetic phase "Egg" was observed. The shape of the spectral line and an additional Raman band at 2558 cm^{-1} may indicate the presence of topaz-OH within the same inclusion.

4. Discussion

4.1. Remarks about the possible existence of an Al-phase in the upper and lower parts of the mantle.

The existence of an Al-phase in the upper and lower parts of the Earth's mantle, i.e. below the Transition Zone is still debated. Although early experimental work on

Table 2
Observed lattice parameters and d_{hkl} values

d_{hkl} (Å) calculated from HREM results (tetragonal)	hkl	d_{hkl} (Å) observed from HREM images	d_{hkl} (Å) observed from electron diffraction pattern	d_{hkl} (Å) phase egg (Schmidt et al., 1998) (monoclinic)	hkl	d_{hkl} (Å) stishovite	hkl
7.435	(100)	7.435	7.322	7.067	(100)	4.177	(100)
7.435	(010)	7.435		4.33	(010)	4.177	(010)
7.06	(001)	7.06	7.087	6.877	(001)	2.666	(001)
		6.05					
		5.57					
5.26	(110)	5.32	5.43	5.333	(10-1)		
5.12	(011)	5.16/5.02	5.025				
4.22	(111)	4.46	4.353				
3.72	(020)	3.76	3.88/3.66	3.695/3.66	(110)/(011)		
3.53	(002)	3.52	3.43	3.53	(200)		
3.32	(120)	3.35	3.31	3.44	(002)		
3.29	(021)	3.26	3.21	3.36	((11-1)		
3.19	(012)						
3.01	(211)		2.95			2.953	(110)
2.93	(112)	2.88	2.87				
			2.74				
2.63	(220)	2.69	2.68	2.74	(210)		
2.56	(022)	2.52	2.55	2.69	(012)/(211)/ (11-2)		
2.46	(221)			2.45	(211)		
2.42	(122)			2.42	(111)		
2.35	(130)			2.33	(30-1)		
2.34	(301)	2.31	2.33	2.30	(202)		
2.27	(311)			2.28	(10-3)		
2.24	(103)		2.24			2.24	(101)
2.08	(30-2)	2.06	2.09			2.09	(200)

The cell parameters of the tetragonal structure were derived from 18 individual HREM images. The d_{hkl} values were measured from fast Fourier Transforms from HREM images of 53 individual nanocrystals and additionally from 13 different electron diffraction patterns.

pyrolite and MORB under lower mantle conditions favoured the existence of an Al-rich phase (Irifune and Ringwood, 1987), subsequent experimental studies suggested an absence of an aluminous phase in the upper part of the Earth's lower mantle, concluding that Al_2O_3 should be accommodated mainly in $MgSiO_3$ perovskite (Irifune, 1994). Another investigation, based on inclusions in diamond, concluded Al_2O_3 to be present as oxide or located in some silicate phase a matter of uncertainty (Harte and Harris, 1994). Porous Al_2O_3 grains were found in a Si rich amorphous matrix together with nanocrystalline diamonds in melt inclusions in a mantle-derived garnet pyroxenite xenolith from Hawaii (Wirth and Rocholl, 2003). Mineral associations in diamond from Sao Luiz, Brazil with aluminous phases such as TAPP, an Al-rich enstatite (former MgSi-perovskite) and an Al_2O_3 phase were described (Harte et al., 1999). However, the authors admitted, it might be possible that Al_2O_3 occurs only in exceptionally aluminous compositions. A recent study of inclusions in diamond from the Sao Luiz area reports an original mineral association of MgSi-perovskite and Al_2O_3 (Hutchison et al., 2001). Phase relations place this assemblage between the lower mantle pressures of 26.5 GPa and about 30 GPa. In a more recent paper on mantle diamonds from Rio Soriso, Brazil one of the figures displays mineral proportion versus pressure, which indicates a stability field for an Al-rich phase labelled with a question mark (Hayman et al., 2005). From experimental studies, as well as from investigations on inclusions in diamond, it must be concluded that the presence or absence of an Al-phase in the upper part of the lower mantle is still a matter of uncertainty.

4.2. Structural discrepancy between synthetic phase "Egg" and the observed hydrous aluminium silicate

The Al:Si X-ray intensity ratio is approximately 1:1 in phase "Egg" as well as in the observed nanophases. There is an OH indicative pre-peak prior to the onset of the oxygen K-edge, which is present in both phases displaying the same intensity (cf. Fig. 6a,b). The only differences in chemical composition are some minor amounts of Fe (in the range of 0.29–1.52 at.% Fe) in the natural nanophases compared to a minor concentration of

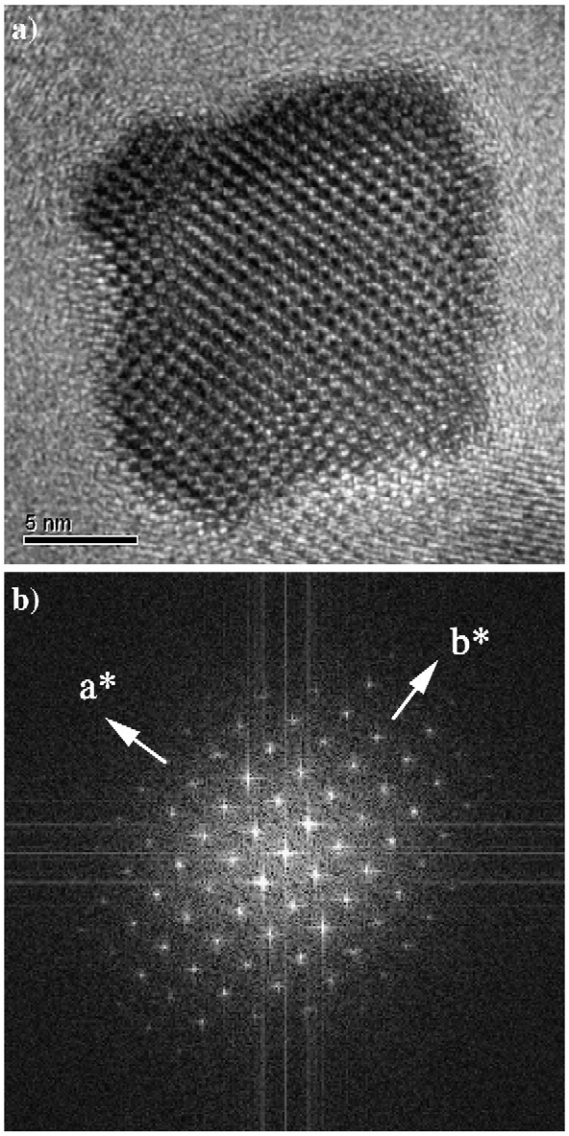

Fig. 8. a) Energy-filtered high-resolution image of a typical idiomorphic nanoinclusions of phase egg. b) Calculated diffraction pattern (FFT) of the same nanocrystal with the major axis of the same length indicated.

Ca (0.42–0.45 at.% Ca) in synthetic phase "Egg". Phase "Egg" material used for crystal structure determination has a maximum CaO concentration of 0.06 wt.% (Schmidt et al., 1998). From a major element chemical point of view there are no significant differences between synthetic phase "Egg" and the observed nanophases. However, the lattice parameters are different. The observed d_{hkl} values do not fit those of monoclinic phase "Egg" (cf. Table 2). Assuming a tetragonal unit cell, the calculated d_{hkl} data fit the observed data much better. In this context, it should be emphasized that there is one nanocrystal observed in the inclusion in diamond that exhibited the monoclinic angle 98.4°, thus indicating a monoclinic cell. The vast majority of the hydrous aluminium silicate nanocrystals studied displays a tetragonal structure.

This observation suggests that nanocrystalline phase "Egg" in the inclusions in diamond crystallized with a tetragonal structure. At lower pressure, during uplift of the diamond and pressure decrease, the tetragonal phase might have partially transformed into a monoclinic structure, the structure of synthetic phase "Egg" that was determined at ambient conditions. A recent paper, based on NMR and Raman studies, reported that the Si–Al distribution in phase "Egg" is partially disordered. However, the monoclinic structure derived from powder XRD assumes an ordered arrangement of SiO_6 and AlO_6 octahedra linked by both edge and corner sharing (Schmidt et al., 1998; Xue et al., 2006). The significance of partial Si–Al disorder was not evaluated in the structural refinement. The observed structural disorder and hydrogen bonding is suggested to be responsible for the high upper temperature limits (1500–1700 °C) of phase "Egg" (Xue et al., 2006). It can be speculated that due to the disorder at high temperatures a tetragonal unit cell might be more favourable from an energetic point of view. Si–Al ordering during cooling might cause a structural change to a monoclinic structure, which has not yet been observed. Additionally, we need to keep in mind that the observed natural phase "Egg" contains a low amount of iron in contrast to Ca in case of the synthetic phase "Egg", and we do not know its influence on the crystal structure. The question arises, why not all of the tetragonal nanocrystals in the inclusions transformed to a monoclinic structure. One reason might be that such disorder-order transformations are very sluggish like in the case of the transformation of the disordered hexagonal cordierite to ordered orthorhombic cordierite (Putnis, 1992). Another reason might be the nanocrystalline state of phase "Egg" itself. Nanocrystalline materials show properties which deviate significantly from those of larger single crystals such as mechanical properties, thermal stability, thermal expansion and electrical resistivity (Gleiter, 1989). In a recent paper on natural nanocrystalline (Mg, Fe, Cr) TiO_3 perovskite nanoinclusions in olivine it is demonstrated that the monoclinic structure stable at high pressure and temperature can be quenched (Wirth and Matsyuk, 2005), whereas synthetic crystalline material of the same composition is not quenchable and structural changes occur (Leinenweber et al., 1995). There is strong evidence that structural phase transformations might be prevented by nanocrystalline grain morphology. For

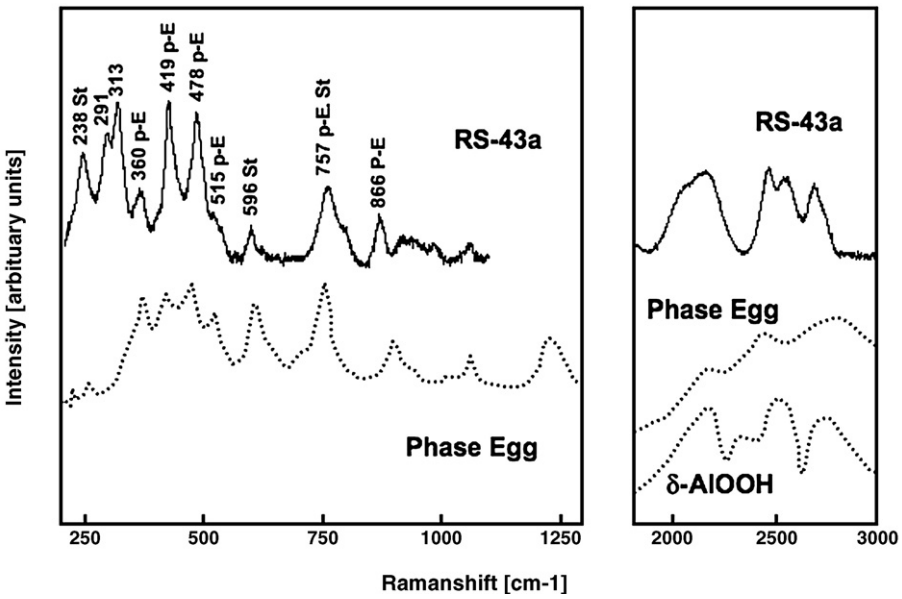

Fig. 9. Raman spectra of a sealed inclusion in diamond RS43-a (solid line) using a 633 nm laser for the shift region between 200 and 1200 cm^{-1} and a 532 nm laser for the OH-stretching region. Values for Raman bands are given on top of each peak and indexed by p-E for phase "Egg" or St for stishovite. Reference spectra for phase Egg and δ-AlOOH are from Xue et al. (2006).

example, the structural phase transformation from γ-Fe to α-Fe in pure iron during cooling of coarse-grained polycrystalline material does not occur in isolated nanometre-sized crystals (Gleiter, 1989). One explanation for such behaviour might be that the nanocrystals do not contain suitable nucleation sites for the α-phase or that growth of the α-phase is inhibited.

4.3. Speculations about the formation of a hydrous aluminium silicate phase such as phase "Egg" under mantle conditions and its preservation

Two different scenarios of the formation of phase "Egg" in the observed inclusions are discussed. Firstly, we consider prograde formation of phase "Egg" in a subducted slab following a path bounded by a cold and hot slab geotherm at the central parts of a slab (Helffrich and Brodholt, 1991; Kirby et al., 1996). Diaspor (α-AlOOH) as an Al-rich and water-carrying phase and SiO_2 phase (quartz, coesite or stishovite) are subducted deep into the upper mantle reaching the Transition Zone at 410 km (c.f. Fig. 10). On its way down, in the stability field of diamond, diamond growth encapsulates diaspor+SiO_2 to form an inclusion. Approaching the 410 km discontinuity diaspor+SiO_2 (stishovite) reacts to form phase "Egg" without release of water. In this case the observed porosity of the inclusions is not explained.

Secondly, we consider retrograde formation of phase "Egg". Again, diaspor+SiO_2 are transported in a downgoing slab along a slab geotherm bounded by a cold and hot slab geotherm (Helffrich and Brodholt, 1991; Kirby et al., 1996). Below the 410 km discontinuity, diaspor+SiO_2 react to phase "Egg". The slab moving further downward

Table 3
Comparison of the peak position of Raman spectra [cm^{-1}]

RS-43a	Phase Egg	δ-AlOOH	Topaz-OH	Stishovite
[633 nm]				
238	255			231
291		280	285	
313				
360	374	385	359	
		402		
419	418	415		
478	474			
515	521	504	504	
596	610	613		589
		640		
757	754			753
866	898		897	
	940			966
	1232		1140	
OH stretching region [532 nm]				
2155	2150	2170		
		2330		
2470	2450			
2558		2530		
2695	2800	2740		
			3525	
			3593	

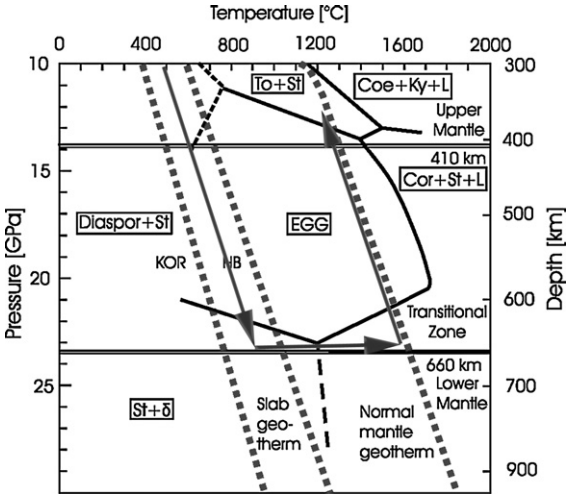

Fig. 10. Schematic depth–temperature diagram with the 410 km and 660 km discontinuities enclosing the mantle transition zone indicated. Phase relations of phase "Egg" together with that of δ-AlOOH (Ono, 1999). The geotherms Helffrich and Brodholt (1991), Kirby et al. (1996) at the centre of the slab and the normal mantle geotherm [Akaogi and Ito, 1993] are given in the figure. A possible path of crustal material in a down-going slab is indicated by arrows.

reaching P–T conditions of $P>23$ GPa and $T<1200$ °C near the 660 km discontinuity, phase "Egg" decomposes into δ-AlOOH + stishovite (Sano et al., 2004). Reaching the 660 km discontinuity the downward movement of the slab may come to a standstill and the temperature of the slab starts rising to finally equilibrate with that of the mantle environment. This scenario is based on a recently calculated density profile of a hypothetical continental crust composed of stishovite:hollandite:majorite = 1:1:1 in volume (Nishiyama et al., 2005). With rising temperature and finally exceeding 1200 °C at 23 GPa δ-AlOOH decomposes to corundum + stishovite + fluid (Fig. 10) (Sano et al., 2004). At that point, we assume that under these conditions diamond forms and during growth incorporates corundum + SiO_2 + fluid. During uplift of the diamond following a normal mantle geotherm, the inclusion composed of corundum + SiO_2 + fluid reacts to form phase "Egg" again. The observed porosity of the inclusion can be easily explained by the presence of the fluid. From the minor concentration of F- P- S- Cl-K- Ca- Ba as quench products at the walls of the pores it can be concluded that the fluid is not pure water. These quench products are similar in its composition to the quench products of a fluid that is commonly present in micro-inclusions (<1 μm) in diamonds from different localities. This composition represents the composition of a high-density fluid (HDF) enriched in incompatible elements (Cl, K, P, Ba and Sr) and water Klein BenDavid et al. (2006).

However, the inclusions described in this paper are not a quench product of a hydrous silica melt phase. The author and co-workers have studied numerous nano- and micro-inclusions in diamond from different locations (such as Siberia, Northern Canada, South Africa and Brazil) containing a hydrous melt phase. Never ever a hydrous Al–Si phase comparing to phase "Egg" was observed. In all the investigated samples we found in the nano- and micro-inclusions in diamond mineral associations of a silicate phase (phlogopite) + carbonate + TiO_2 phase (rutile or ilmenite) + NaCl/KCl + apatite and in some cases even sulfide. None of these investigated diamonds was a "superdeep" diamond. Some of these results have recently been published Klein BenDavid et al. (2006) and others are in preparation or have been submitted.

From our many observations on nanoinclusions in diamond we conclude that the inclusion composed of phase "Egg" + stishovite + quench phase described in the present paper represents an inclusion in diamond that has not yet been reported.

Acknowledgement

Bernd Wunder is thanked for providing synthetic phase "Egg". Critically reading a first draft of the manuscript by Wilhelm Heinrich is acknowledged. Ian Coulson is thanked for his help in editing of the manuscript. The drawing of Fig. 9 by Stephan Augustin is greatfully acknowledged. Financial support by the Deutsche Forschungsgemeinschaft DFG (436UKR 17/26/05) is gratefully acknowledged. A review of an earlier draft of the manuscript by L. Dobrzhinetskaya helped to improve the present manuscript.

Appendix A. Supplementary data

Supplementary data associated with this article can be found, in the online version, at doi:10.1016/j.epsl.2007.04.041.

References

Akaogi, M., Ito, E., 1993. Refinement of $MgSiO_3$ perovskite and negative pressure–temperature slopes for perovskite-forming reactions. Geophysical Research Letters 20, 1839–1842.

Brenker, F.E., Stachel, T., Harris, J.W., 2002. Exhumation of lower mantle inclusions in diamonds — ATEM investigation of retrograde phase transitions, reactions and exsolution. Earth and Planetary Science Letters 198, 1–9.

Brenker, F.E., Vincze, L., Vekemans, B., Nasdala, L., Stachel, T., Vollmer, C., Kersten, M., Somogyi, A., Adams, F., Joswig, W., Harris, J.W., 2005. Detection of a Ca-rich lithology in the Earth's deep (>300 km) convecting mantle. Earth and Planetary Science Letters 236, 579–587.

Davies, R., Griffin, W.L., Pearson, N.J., Andrew, A., Doyle, B.J., O'Reilly, S.Y., 1999. Diamonds from the deep: Pipe DO-27, Slave Craton, Canada. In: Gurney, J.J., Gurney, J.L., Pascoe, M.D., Richardson, S.H. (Eds.), Proceedings of the VIIth International Kimberlite Conference. Red Roof Design, Cape Town, vol. 1, pp. 148–155.

Eggleton, R.A., Boland, J.N., Ringwood, A.E., 1978. High-pressure synthesis of a new aluminium silicate: $Al_5Si_5O_{17}(OH)$. Geochemical Journal 12, 191–194.

Gleiter, H., 1989. Nanocrystalline materials. Progress in Materials Science 33, 223–315.

Harris, J., Hutchison, M.T., Hursthouse, M., Light, M., Harte, B., 1997. A new tetragonal silicate mineral occurring as inclusions in lower-mantle diamonds. Nature 387, 486–488.

Harte, B., Harris, J.W., 1994. Lower mantle mineral associations preserved in diamonds. Mineralogical Magazine 58A, 384–385.

Harte, B., Harris, J.W., Hutchison, M.T., Watt, G.R., Wilding, M.C., 1999. Lower mantle mineral associations in diamonds from Sao Luiz, Brazil. In: Fei, Y., Bertka, C.M., Mysen, B.O. (Eds.), Mantle Petrology: Field Observations and High Pressure Experimentation: A tribute to Francis R (Joe) Boyd. Geochemical Society Spec. Publ., vol. 6, pp. 125–153.

Hayman, P.C., Kopylova, M.G., Kaminsky, F.V., 2005. Lower mantle diamonds from Rio Soriso (Juina area, Mato Grosso, Brazil). Contributions to Mineralogy and Petrology 149 (4), 430–445.

Helffrich, G., Brodholt, J., 1991. Relationship of deep seismicity to the thermal structure of subducted lithosphere. Nature 353, 252–255.

Hutchison, M.T., Hurtshouse, M.B., Light, M.E., 2001. Light, mineral inclusions in diamonds: associations and chemical distinctions around the 670-km discontinuity. Contributions to Mineralogy and Petrology 142 (2), 119–126.

Irifune, T., 1994. Absence of an alumious phase in the upper part of the Earth's lower mantle. Nature 370, 131–133.

Irifune, T., Ringwood, A.E., 1987. Phase transformations in primitive MORB and pyrolite compositions to 25 GPa and some geophysical implications. In: Manghnani, M.H., Syono, Y. (Eds.), High pressure research in mineral physics. Terrapub, Tokyo, pp. 231–242.

Kaminsky, F.V., Zakharchenko, O.D., Griffin, W.L., Channer, D.M.DeR., Khachatryan-Blinova, G.K., 2000. Diamonds from the Guaniamo area, Venezuela. Canadian Mineralogist 38 (6), 1347–1370.

Kaminsky, F.V., Zakharchenko, O.D., Davies, R., Griffin, W.L., Shiryaev, A.A., 2001. Superdeep diamonds from the Juina area, Mato Grosso State, Brazil. Contributions to Mineralogy and Petrology 140 (5), 734–753.

Kaminsky, F.V., Zakharchenko, O.D., Khachatryan, G.K., Griffin, W.L., Channer, D.M.DeR., 2006. Diamond from the Los Coquitos Area, Bolivar State, Venezuela. Canadian Mineralogist 44 (2), 661–678.

Kirby, S.H., Stein, S., Okal, A., Rubie, D.C., 1996. Metastable mantle phase transformations and deep earthquakes in subducting oceanic lithosphere. Reviews of geophysics 34, 261–306.

Klein BenDavid, O., Wirth, R., Navon, O., 2006. TEM imaging and analysis of microinclusions in diamond: a close look at diamond-growing fluids. American Mineralogist 91, 353–365.

Leinenweber, K., Linton, J., Navrotsky, A., Fei, Y., Parise, J.B., 1995. High-pressure perovskites on the join $CaTiO_3$–$FeTiO_3$. Physics and Chemistry of Minerals 22, 251–258.

Nishiyama, N., Rapp, R.P., Irifune, T., Sanehira, T., Yamazaki, D., Funakoshi, K., 2005. Stability and P–V–T equation of state of $KAlSi_3O_8$-hollandite determined by in situ X-ray observations and implications for dynamics of subducted continental crust material. Physics and Chemistry of Minerals 32, 627–637.

Okay, A.I., 1993. Petrology of a diamond and coesite-bearing metamorphic terrain — Dabie Shan, China. European Journal of Mineralogy 5, 659–675.

Ono, S., 1999. High temperature stability limit of phase "Egg", $AlSiO_3$ (OH). Contributions to Mineralogy and Petrology 137, 83–89.

Otter, M.L., Gurney, J.J, 1989. Mineral inclusions in diamonds from Sloan diatremes, Colorado–Wyoming State Line kimberlite district, North America. In: Ross, J., Jaques, A.L., Ferguson, J., Green, D.H., O'Reilly, S.Y., Danchin, R.V., Janse, A.J.A. (Eds.), Kimberlites and related rocks [Geol. Soc. Australia Spec. Publ. 14]. Proceedings of the Fourth International Kimberlite Conference, Perth 1986., vol. 2. Blackwell, Carlton, pp. 1042–1053.

Putnis, A., 1992. Introduction to Mineral Sciences. Cambridge University Press, p. 457.

Sano, A., Ohtani, E., Kubo, T., Funakoshi, K., 2004. situ X-ray observation of decomposition of hydrous aluminium silicate $AlSiO_3(OH)$ and aluminium oxide hydroxide δ-AlOOH at high pressure and temperature. Journal of Physics and Chemistry of Solids 65, 1547–1554.

Schmidt, M.W., Finger, L.W., Ross, R.J., Dinnebier, R.E., 1998. Synthesis, crystal structure, and phase relations of $AlSiO_3OH$, a high-pressure hydrous phase. American Mineralogist 83, 881–888.

Scott-Smith, B.H., Danchin, T.V., Harris, J.W., Stracke, K.J., 1984. Kimberlites near Orroroo, South Australia. In: Kornprobst, J. (Ed.), Kimberlites II: The Mantle and Crust–Mantle Relationships. Elsevier, Amsterdam, pp. 121–142.

Stachel, T., Harris, J.W., Brey, G.P., Joswig, W., 2000. Kankan diamonds (Guinea) II: lower mantle inclusion paragenesis. Contributions to Mineralogy and Petrology 140 (1), 16–27.

Vanpeteghem, C.B., Ohtani, E., Kondo, T., Takemura, K., Kiregawa, T., 2003. Compressibility of phase "Egg" $AlSiO_3OH$: equation of state and role of water at high pressure. American Mineralogist 88, 1408–1411.

Wilding, M.C., Harte, B., Harris, J.W., 1991. Evidence for a deep origin for the Sao Luiz diamonds. Fifth International Kimberlite Conference Extended Abstracts, Araxa, June, pp. 456–458.

Wirth, R., 1997. Water in minerals detectable by electron energy-loss spectroscopy EELS. Physics and Chemistry of Minerals 24, 561–568.

Wirth, R., 2004. Focused Ion Beam (FIB): A novel technology for advanced application of micro- and nanoanalysis in geosciences and applied mineralogy. European Journal of Mineralogy 16, 863–876.

Wirth, R., Rocholl, A., 2003. Nanocrystalline diamond from the Earth's mantle underneath Hawaii. Earth and Planetary Science Letters 211, 357–369.

Wirth, R., Matsyuk, S., 2005. Nanocrystalline (Mg, Fe, Cr)TiO_3 perovskite inclusions in olivine from a mantle xenolith, Udachnaya-East kimberlite pipe, Siberia. Earth and Planetary Science Letters 233, 325–336.

Wunder, B., Medenbach, O., Krause, W., Schreyer, W., 1993a. Synthesis, properties and stability of $Al_3Si_2O_7(OH)_3$ (phase pi), a hydrous high-pressure phase in the system Al_2O_3–SiO_2–H_2 (ASH). European Journal of Mineralogy 5, 637–649.

Wunder, B., Rubie, D.C., Ross, C.R., Medenbach, O., Seifert, F., Schreyer, W., 1993b. Synthesis, stability, and properties of $Al_2SiO_4(OH)_2$: a fully hydrated analogue of topaz. American Mineralogist 78, 285–297.

Xue, X., Kanzaki, M., Fukui, H., Ito, E., Hashimoto, T., 2006. Cation order and hydrogen bonding of high-pressure phases in the Al_2O_3–SiO_2–H_2O system: an NMR and Raman study. American Mineralogist 91, 850–861.